The SOMA Atomic Outflow Survey. I. An Atomic O I and Highly Ionized O III Outflow from Massive Protostar G11.94-00.62

The Astrophysical Journal, 1003:26 (14pp), 2026 May 20 https://doi.org/10.3847/1538-4357/ae5485

The SOMA Atomic Outflow Survey. I. An Atomic O I and Highly Ionized O III Outflow from Massive Protostar G11.94-00.62

Phillip Oakey[1], Yao-Lun Yang[2], Jonathan C. Tan[1,3], Thomas G. Bisbas[4], Rubén Fedriani[5], Kei E. I. Tanaka[6], Zoie Telkamp[1], Yichen Zhang[7], Christian Fischer[8], and Lianis Reyes Rosa[1]
[1] Department of Astronomy, University of Virginia, Charlottesville, VA, 22904, USA; rxr4nd@virginia.edu, jonathan.tan@chalmers.se
[2] Star and Planet Formation Laboratory, RIKEN Pioneering Research Institute, Wako-shi, Saitama, 351-0106, Japan; yao-lun.yang@riken.jp
[3] Department of Space, Earth, and Environment, Chalmers University of Technology, Gothenburg, Västra Götaland, 412 96, Sweden
[4] Research Center for Computational Earth and Space Science, Zhejiang Lab, Hangzhou, Zhejiang Province, 311121, People's Republic of China
[5] Instituto de Astrofísica de Andalucía, CSIC, Glorieta de la Astronomía s/n, E-18008 Granada, Spain
[6] Department of Earth and Planetary Sciences, Institute of Science Tokyo, Meguro, Tokyo, 152-8551, Japan
[7] Department of Astronomy, Shanghai Jiao Tong University, 800 Dongchuan Rd., Minhang, Shanghai 200240, People's Republic of China
[8] IRAM—Institut de Radioastronomie Millimétrique, 300 rue de la Piscine, 38406, Saint-Martin d'Hères, France
Received 2025 September 24; revised 2026 March 17; accepted 2026 March 17; published 2026 May 12

Abstract

Massive stars regulate galaxy evolution and star formation through their physical and chemical feedback, but their formation remains poorly understood. Accretion-powered outflows provide important diagnostics of massive star formation. We present first results from the SOMA Atomic Outflow Survey, a far-infrared massive star formation survey using the FIFI-LS instrument on SOFIA. We report the detection of [O III] $^3P_2 \rightarrow {}^3P_1$ emission at 52 μm from the massive protostar G11.94-0.62, tracing highly ionized gas. We also detect [O I] $^3P_2 \rightarrow {}^3P_1$ and $^3P_1 \rightarrow {}^3P_0$ at 63 and 145 μm tracing atomic gas, as well as CO $J = 14 \rightarrow 13$ at 186 μm from highly excited molecular gas. The [O III] and [O I] lines exhibit large line widths ($\sim$200 and $\sim$40–80 km s^{-1}, respectively) and their morphologies are consistent with a wide-angle bipolar outflow. The properties of molecular tracers (^{12}CO, ^{13}CO, C^{18}O, H_2CO, and CH_3OH) observed with the Atacama Large Millimeter/submillimeter Array support this interpretation. Ionized nebula and photodissociation region modeling imply an ionized outflow mass flux of $\sim 8 \times 10^{-5}\, M_\odot\, \mathrm{yr}^{-1}$ and an atomic outflow mass flux of $\sim 5 \times 10^{-6}\, M_\odot\, \mathrm{yr}^{-1}$, while the molecular outflow traced by CO has an implied mass flux of $\sim 3 \times 10^{-4}\, M_\odot\, \mathrm{yr}^{-1}$. The mass and momentum flux in the ionized outflow are consistent with the primary disk wind, while the molecular component is mainly swept-up, secondary outflow gas. We also observe G11.94-0.62 with the Large Binocular Telescope in the near-infrared, potentially tracing the base of wide-angle outflow cavities. Spectral energy distribution modeling implies a protostellar mass $m_* = 22.4^{+21}_{-11}\, M_\odot$, while the [O III] emission implies $m_* \gtrsim 30\, M_\odot$ and that the protostar is in the final stages of its accretion.

Unified Astronomy Thesaurus concepts: Star formation (1569); Massive stars (732); Jets (870); Photodissociation regions (1223)

1. Introduction

Massive stars impact many aspects of the evolution of galaxies, the interstellar medium, and star and planet formation (H. Beuther 2007; J. C. Tan et al. 2014). However, determining the formation processes of massive stars is often challenging due to the presence of complex, high column density gas and dust structures and the large distances to the sources. Bipolar protostellar outflows, ubiquitous in both low- and high-mass star-forming regions, provide an important window to constrain the properties of protostars (J. Bally 2016). The low-density, low-extinction outflow cavities can enable observations at shorter, near-IR (NIR) and mid-IR (MIR) wavelengths, to probe into the inner regions of protostellar cores. In addition, the kinematics of these accretion-powered outflows, e.g., their mass and momentum flux, can serve as important diagnostics for understanding protostellar accretion. Finally, understanding the outflows in their own right is important since they likely regulate the local star formation efficiency from the massive protostellar core and help regulate surrounding star formation activity in the protocluster clump.

One key difference of massive protostars compared to their lower-mass counterparts is the potential for much stronger far- and extreme-ultraviolet (FUV and EUV) radiation. This phenomenon is expected to become important in the phase when massive protostars contract to near the zero-age main sequence (ZAMS) while still accreting, which is theorized to occur for the most massive sources ($m_* \gtrsim 20\, M_\odot$) (Y. Zhang et al. 2014). Irradiated by FUV and EUV photons, outflowing gas can be dissociated and ionized, producing strong lines that diagnose atomic and ionized phases (e.g., K. E. I. Tanaka et al. 2016). Thus, studying protostars exhibiting such ionized and atomic outflows is important for understanding massive star formation at the onset of powerful radiative feedback.

G011.94-00.62 (hereafter G11.94) is an ultracompact (UC) H II region whose morphology was first described by D. O. S. Wood & E. Churchwell (1989). We adopt a distance of 4.02 kpc and a v_{lsr} of 37.0 km s^{-1} (M. Wienen et al. 2015). From Very Large Array (VLA) 2 and 6 cm images, D. O. S. Wood & E. Churchwell (1989) identified a parabolic "cometary" ionization front that peaks toward the SW side of

the protostar. Early observations at millimeter wavelengths found compact dust emission without a clear structure (S. Watt & L. G. Mundy 1999). Wide-field Midcourse Space Experiment (MSX) observations in the MIR (6–25 μm) identified a slight elongation to the NW and SE and also detected a faint source 70″ to the SW (P. A. Crowther & P. S. Conti 2003). A similar NW–SE elongation is seen in MIR Infrared Telescope Facility (IRTF)/MERLIN observations at 11.7 and 20.8 μm (J. M. De Buizer et al. 2003), but the MIR and radio emission have different brightness peaks and the cometary shape seen in radio observations is missing in the MIR images. Q.-F. Zhu et al. (2008) presented the distribution of the [Ne II] 12.8 μm line, showing a broad line width with most [Ne II] emission appearing within $v_{\rm lsr} = 30-60$ km s^{-1}. However, a detailed kinematic analysis was challenged by the complex morphology of the system.

P. Hofner & E. Churchwell (1996) reported two regions of water maser emission, located ∼3″ SW and ∼10″ W of the UC H II region. They found both masers to be located to the W of the large cometary arc. Both water maser locations were later found to have corresponding MIR sources (J. M. De Buizer et al. 2003). A. J. Walsh et al. (2003) associated a methanol maser with one of the water maser sites.

Regarding molecular emission, a single-pointing ^{12}CO $J = 1 \rightarrow 0$ observation by D. S. Shepherd & E. Churchwell (1996) shows a broad full-width zero-intensity line width greater than 28.5 km s^{-1}, consistent with that seen in [Ne II], indicating the presence of an outflow. Single-dish observations of ^{13}CO $J = 1 \rightarrow 0$ also found a broad line with three peaks, suggesting complex structure within the single-dish beam of 22″ (E. Churchwell et al. 1992).

In this paper, we present observations of atomic and ionized outflows in G11.94, taken with the FIFI-LS instrument on board SOFIA. In Section 2, we describe our FIFI-LS observations and reduction process, as well as discuss archival Atacama Large Millimeter/submillimeter Array (ALMA) data and new Large Binocular Telescope (LBT) imaging which supplements our SOFIA observations. In Section 3, we present the spectra for the [O I] 63 μm and 145 μm lines, the [O III] 52 μm line, and the CO $J = 14-13$ line at 186 μm. We then present the morphologies for each line as well as the associated continua. In Section 4, we present a discussion on the outflow position angle (P.A.), kinematics, and origins of the detected species, as well as the [O I] mass-loss (outflow) rate estimated using non-LTE radiative transfer calculation and photodissociation region (PDR) modeling. We also refer here to ALMA data for estimates of the molecular outflow. In Section 5, we discuss the implications of our results and present our conclusions.

2. Observations

2.1. SOFIA FIFI-LS

Observations were taken using the Far-infrared, Field-imaging Line Spectrometer (R. Klein et al. 2014; S. Colditz et al. 2018; C. Fischer et al. 2018) attached to the 2.5 m mirror (aperture) on board the Stratospheric Observatory for Infrared Astronomy (SOFIA; P. Temi et al. 2018). The program (project ID 09_0169; PI: Y.-L. Yang) covers 18 massive protostars selected from the larger sample of the SOFIA Massive (SOMA) Star Formation Survey (PI: J. C. Tan) to survey the emission of the [O I] $^3P_2 \rightarrow {}^3P_1$ and $^3P_1 \rightarrow {}^3P_0$ transitions at 63.18 and 145.5 μm (L. R. Zink et al. 1991), the [O III] $^3P_2 \rightarrow {}^3P_1$ transition at 51.81 μm (C. Froese Fischer & H. P. Saha 1985), and the CO $J = 14 \rightarrow 13$ line at 185.99 μm (B. Yang et al. 2010). For brevity, we will hereafter refer to these lines as [O I] 63 and 145 μm, [O III] 52 μm, and CO 186 μm, respectively. In this work, we report the SOFIA/FIFI-LS data on G11.94. The observations were taken on 2021 June 3, with exposure lengths (on-source) of 460.8 s for the 63–145 μm bandpair and 307.2 s for the 52–186 μm bandpair.

FIFI-LS is an integral field unit comprised of two spectrometers, capable of observing the same region simultaneously at two wavelength channels using a dichroic. The short-wavelength channel covers wavelengths of 51–120 μm and the long-wavelength channel covers 115–200 μm. Both detectors in the short- and long-wavelength channels have 5 × 5 spatial pixels with a size of 6″ and 12″, respectively, and 16 spectral pixels each. Thus, the short- and long-wavelength channels have an instantaneous field of view (FoV) of 30″ × 30″ and 60″ × 60″ with beam sizes of 6.″6, 7.″4, 14.″1, and 18.″1 in the 52, 63, 145, and 186 μm ranges. We set up two observations in which each bandpair (63 + 145 μm and 52 + 186 μm) was simultaneously observed. In our observations, we used the D130 and D105 dichroics to maximize the throughput at 52 and 63 μm, respectively. The velocity resolution of FIFI-LS is 320, 230, 280, and 200 km s^{-1} in the 52, 63, 145, and 186 μm ranges, respectively (D. Fadda et al. 2023). The instantaneous spectral coverage is 1000–3000 km s^{-1} in the short-wavelength channels and 800–2500 km s^{-1} in the long-wavelength channels.

The data were processed with version 2.9.0 of the FIFI-LS pipeline provided by the SOFIA Science Center and the atmospheric correction with ATRAN (S. D. Lord 1992) outlined by C. Fischer et al. (2021) and C. Iserlohe et al. (2021). The pipeline uses a 3D fitting method to bin the data, which rejects data points from bad fits. This affects the edge shape of the reduced maps due to lower integration times there caused by dithering (C. Fischer et al. 2016) during the mapping (see panels (VI) and (VIII) in Figure 1). There are known telluric features in all of the channels (except for 186 μm), and our methods for handling these features are explained throughout the paper. In the 52 μm channel, this manifests as a large peak to the blue side of the line, beginning roughly around −400 km s^{-1} and extending beyond (see Figure 2). This region was excluded from line measurements, and we manually avoided selecting any wavelength from it for measuring the continuum. The 145 μm band (panel (VIII)) features a small "bump" around −500 km s^{-1} and similarly this region of the spectrum was excluded from inclusion in any analysis, including continuum selection. The situation for the 63 μm spectrum (panel (VI)) is slightly different. The telluric feature convolves directly with the line on the red wing of the spectrum. Our methods for resolving this contamination are outlined in Section 3.2.

2.2. ALMA

We also obtained archival ALMA data to investigate the nature of the emission lines detected in our FIFI-LS observations (discussed in Section 4.2). The ^{12}CO data were taken as part of the QUARKS program (2021.1.00095.S; PIs: L. Zhu, G. Gary, and T. Liu; X. Liu et al. 2024), using the 12 m array in the C-2 and C-5 configurations, as well as the Atacama Compact Array 7 m array (F. Xu et al. 2024). The calibrated visibilities of these data were combined using CASA 6.6.0 (CASA Team et al. 2022) and deconvolved together. The details of the reduction and

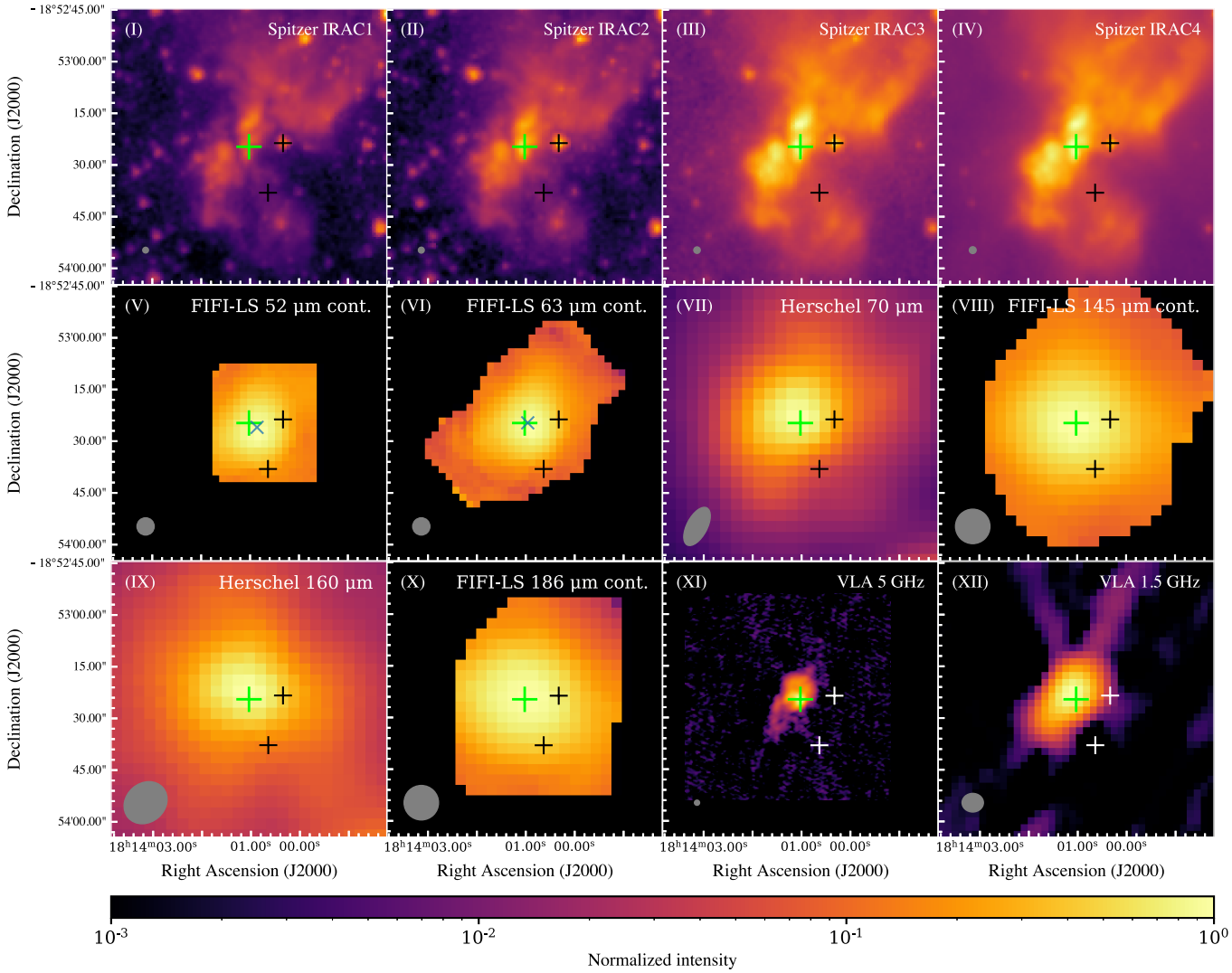

Figure 1. Continuum images of G11.94 from the various wavelengths observed by SOFIA FIFI-LS (this work), Spitzer (E. Churchwell et al. 2009), Herschel (S. Molinari et al. 2016; ObsIDs: 1342218999, 1342219000), and VLA (R. H. Becker et al. 1994; M. G. Hoare et al. 2012; C. R. Purcell et al. 2013). The images are shown in logarithmic scale, normalized to the highest flux in an 80″ × 80″ region centered on the source peak. The green cross denotes the source identified as the G11.94 protostar from ALMA continuum. The two black crosses (white in panels (XI) and (XII) for clarity) are secondary protostars in the region (both detected with ALMA; see Section 4.2). Panels (V) and (VI) also show the peak of emission at 52 and 63 μm (blue "×" symbols). The offset between green "+" and blue "×" helps define the "color gradient" (see text). Beam sizes are shown on the bottom left of each panel.

imaging processes are discussed in X. Liu et al. (2024). The synthesized beam is ∼0.″3 with a sensitivity of ∼6 mJy beam^{-1}. The other ALMA data were taken as part of the ALMAGAL (ALMA Evolutionary Study of High Mass Protocluster Formation in the Galaxy) program (2019.1.00195.L; PI: S. Molinari; S. Molinari et al. 2025) and the imaging products were gathered from the ALMA Science Archive without further calibration and imaging. Four spectral windows were set up in the ALMA observations of G11.94, covering frequencies of 216.960–218.832, 218.037–218.505, 219.032–220.905, and 220.337–220.805 GHz with a channel width of 488, 122, 488, and 122 kHz, respectively. The synthesized beam sizes are (1.″31–1.″37) × (1.″06–1.″08). The sensitivity is ∼6 mJy beam^{-1}.

2.3. LBT

Observations were conducted on 2025 July 24 and 26, using the LBT in binocular mode, which allows for simultaneous use of both mirrors. The data were collected with the LUCI (LBT Utility Camera in the Infrared; W. Seifert et al. 2003) instrument operating in seeing-limited conditions as part of program UV-2025A-03 (PI: J. C. Tan). The N3.75 camera was employed, offering an FoV of 4′ × 4′ and a pixel scale of 0.12″. On LUCI1, installed on the SX (left) mirror, observations were made using the K and Brγ filters (centered at 2.194 and 2.170 μm, respectively). LUCI2, mounted on the DX (right) mirror, used the K and H_2 filters (centered at 2.194 and 2.124 μm, respectively). The images are centered at R.A. (J2000) = 18:14:01.100 and decl.(J2000) = −18:53:23.53, with a P.A. of 270°. Exposure times are 300 s for the K band and 600 s for the Brγ and H_2 narrowband filters. Data reduction followed standard procedures, including sky subtraction and flat-fielding, using custom Python routines based on the ccdproc (M. Craig et al. 2022), astropy (Astropy Collaboration et al. 2022), and photutils (L. Bradley 2023) packages. Final images were aligned and calibrated astrometrically by crossmatching stellar positions with the Two Micron All Sky Survey catalog (M. F. Skrutskie et al. 2006).

3. Results

Using SOFIA/FIFI-LS, we obtained a spectral cube at each line. Massive protostellar cores such as G11.94 emit strong continuum emission at far-IR wavelengths (e.g., J. M. De Buizer et al. 2017; M. Liu et al. 2019, 2020; R. Fedriani et al. 2023; Z. Telkamp et al. 2025). To isolate the emission lines, we need to first measure the continuum at each channel and subtract it from the spectral cubes. In this section, we present the results on continuum imaging/flux measurements in Section 3.1 and various line emission science in Section 3.2.

3.1. Continuum

We measured the continuum from the line-free wavelengths in the bandwidth of each channel. Thus, we selected continuum ranges from outside of 300 km s^{-1} of the source $v_{\rm lsr}$ surrounding the line. The exclusion zone is to ensure there is no contamination from line emission in the continuum, particularly due to the relatively limited spectral resolution of FIFI-LS. We also only selected continuum from where atmospheric interference is at a minimum. This means excluding continuum selection from the blue side of the spectra in [O III] and the red side in [O I] 63 μm due to telluric features, and partially excluding regions from the blue side of the spectra in [O I] 145 μm. Specifically, the continuum was selected from the following ranges (relative to the line center; all in km s^{-1}): 52 μm: 450 to 1050; 63 μm: −650 to −300; 145 μm: −450 to −350 and 350 to 1000; 186 μm: −550 to −300 and 350 to 450. Then, for each pixel, we measured the average flux density within the selected wavelengths for the continuum, deriving a continuum image. These continuum images were later subtracted from the corresponding spectral cubes at each wavelength to produce line-only spectral cubes for line analysis.

3.1.1. Astrometric Correction

We further compared the FIFI-LS continuum images at 52, 63, 145, and 186 μm with archival data on G11.94, including images from the Spitzer Space Telescope (Spitzer), the Herschel Space Observatory (Herschel), the VLA, and ALMA. To provide an accurate comparison, we needed to ensure the astrometry of the FIFI-LS images is consistent with other images. To do so, we first fit a 2D Gaussian profile onto the ALMA continuum image at 218.935 GHz, determining the continuum peak position at (R.A.: $18^{\rm h}14^{\rm m}01\overset{\rm s}{.}00$, decl.: −18° 53′24.″96). We also used this ALMA continuum peak as the source position in the rest of the analyses. Then, we fit a 2D Gaussian profile to each FIFI-LS continuum image to determine the peak positions. To align the images, we only offset the fitted FIFI-LS continuum peak at the two long-wavelength channels (145 and 186 μm) to match the position of the ALMA continuum peak. Because each pair of short- and long-wavelength channels was observed simultaneously, we applied the offsets of the long-wavelength channels to the corresponding short-wavelength channels. The rationale for correcting the long-wavelength channel instead of the short-wavelength channel is that the dust is more optically thin at longer wavelengths, and the continuum at shorter wavelengths could be affected by selective extinction due to asymmetric source structures.

The simultaneous observations of the short- and long-wavelength channels also provide a unique opportunity to study the effect of this selective extinction. If there is a dominant bipolar outflow, we expect a lower extinction at the blueshifted outflow lobe and a higher extinction at the redshifted outflow lobe, resulting in the continuum peak shifting toward the blueshifted outflow at shorter wavelengths (Y. Zhang & J. C. Tan 2011). We derived the "relative offset" between the continuum peaks at the short- and long-wavelength channels of the same observing pair to quantify this selective extinction effect, the P.A. ($\rm PA_{cont}$) of which could also serve as an indicator of outflow direction (see further discussion in Section 4.5).

Figure 1 shows the FIFI-LS continuum images along with archival photometric images from 3.6 μm to 20 cm. The relative offsets are shown as blue crosses in panels (V) and (VI). The 63–145 μm relative offset and P.A. are $1\overset{''}{.}0 \pm 0\overset{''}{.}3$ and $-88\overset{\circ}{.}5 \pm 19\overset{\circ}{.}3$ and the 52–186 μm relative offset and P.A. are $2\overset{''}{.}5 \pm 0\overset{''}{.}5$ and $-126\overset{\circ}{.}2 \pm 12\overset{\circ}{.}4$.

3.1.2. Continuum Measurements

The spectral energy distribution (SED) of massive protostellar sources typically peaks at ∼100 μm because of the abundant relatively cool dust (∼20−100 K) in the envelopes. Thus, the continuum fluxes at 50–200 μm, probed by the FIFI-LS observations, also constrain the SED of G11.94 and further constrain the properties of the dominant protostar by SED modeling (Section 4.1). To estimate the continuum flux for modeling, we first need to determine an aperture that best encompasses the emission of the entire protostellar core. We followed the approach developed in R. Fedriani et al. (2023), which uses the Herschel 70 μm image to determine the aperture where a 30% increase of aperture radius leads to a less than 10% increase of flux. Following this criterion, the optimal aperture radius is $30\overset{''}{.}0$.

The measurement of continuum flux also follows the approach in R. Fedriani et al. (2023). A background-subtracted flux is measured using the 30″ aperture, utilizing `SedFluxer` from the Python package `sedcreator`, while the background is measured from an annulus between one and two aperture radii ($r = 30''-60''$). We applied this approach to the continuum images at Spitzer IRAC bands (3.6, 4.5, 5.8, and 8.0 μm), Wide-field Infrared Survey Explorer Band 3 and 4 at 12 and 22 μm, four wavelengths of the FIFI-LS observations presented in this study, Herschel PACS 70 and 160 μm (which can be seen in panels (VII) and (IX) in Figure 1), and Herschel SPIRE 250, 350, and 500 μm. In the 145 and 186 μm channels, the aperture size is comparable to the FoV of the long-wavelength channel, which is only a few pixels smaller after masking out the bad pixels. However, the FoV at 52 and 63 μm is substantially smaller than the aperture. Thus, we interpolated the area outside the FoV of the short-wavelength channel using the Herschel 70 μm to estimate the continuum flux within the aperture. This was accomplished by reprojecting the Herschel 70 μm image to the FIFI-LS pixel size/orientation, and then calculating the proportion of fluxes within the FIFI-LS FoV in both images. The Herschel 70 μm image was then scaled using this factor, where FIFI-LS data is not present. It is seen from our larger survey sample that this slightly overestimates flux at these two wavelengths and as such, the 52 and 63 μm fluxes were treated as upper limits in our SED fits. We similarly interpolated data from Herschel 160 μm to FIFI-LS 145 and 186 μm measurements. Due to the larger FoV of these long-wavelength images, this

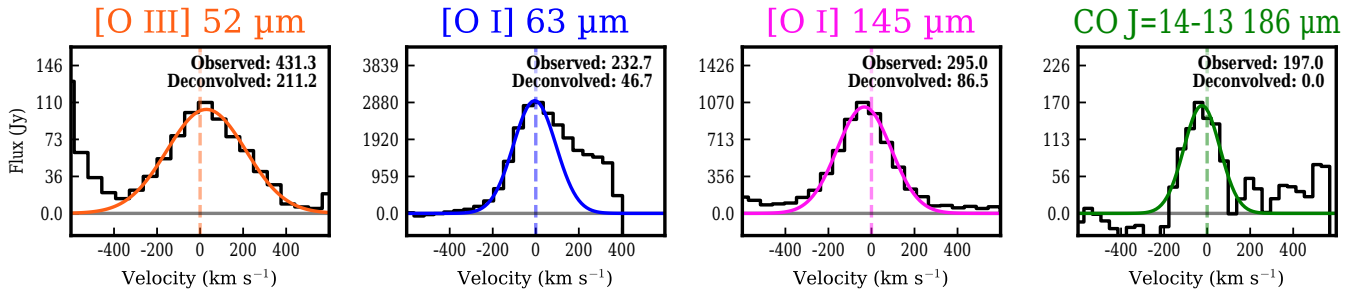

Figure 2. Continuum-subtracted spectra of [O III] $^3P_2 \rightarrow {}^3P_1$ at 51.81 μm, [O I] $^3P_2 \rightarrow {}^3P_1$ and $^3P_1 \rightarrow {}^3P_0$ at 63.18 and 145.5 μm, and the CO $J = 14 \rightarrow 13$ line at 185.99 μm. The velocity is corrected for the source $v_{\rm lsr}$ of 36.2 km s^{-1}. The fitted Gaussian lines are shown. For [O I] in the 63 μm bandpass, the Gaussian profile is fitted over a partial range due to telluric contamination on the red wing. Observed line FWHMs (in km s^{-1}) are written on the top right of each panel, as well as FWHMs deconvolved from the intrinsic instrument FWHM. The intrinsic width of the CO line cannot be ascertained via deconvolution and is listed as zero. Flux tickmarks are plotted in 33% increments of the peak line flux.

interpolation only is relevant for small fractions of the annulus. FIFI-LS continuum measurements can be found in Table 1.

We estimated the uncertainties of all the continuum fluxes following the treatment described in R. Fedriani et al. (2023). Specifically, for background-subtracted fluxes of the protostar that were used in SED fitting we needed to estimate the uncertainty in the background flux. At wavelengths $\geqslant$100 μm the uncertainty in the background flux was assumed to be equal to the level of background flux itself, reflecting the fact that the background is relatively cold, clump material that can dominate over the protostellar core emission. However, at wavelengths $<$100 μm the uncertainty in the background flux was assumed to be given by the level of variation seen in aperture-sized regions immediately around the source, which was derived using `SedFluxer`. The uncertainty in background flux was then added in quadrature with an assumed 10% of the background-subtracted flux (C. Fischer et al. 2018) to derive the total uncertainty. The SED and the properties inferred from the SED modeling are discussed in Section 4.1, and the model fitting is visualized in Figure 3.

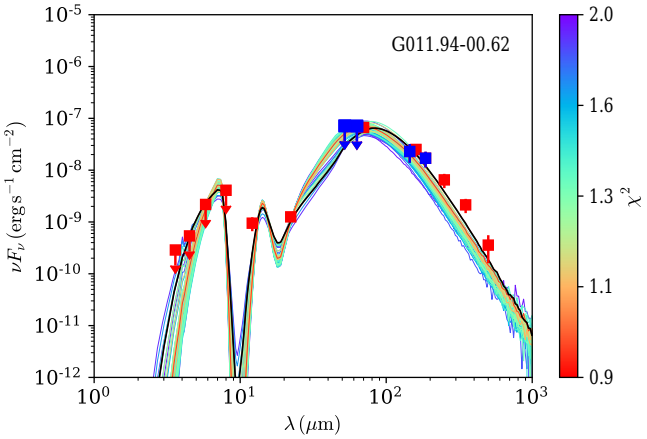

Figure 3. SED for G11.94. The blue data points are measured by FIFI-LS, while the red points are from other observatories. The black line represents the best-fit model, with a χ^2 value of 0.85.

3.2. Line Emission

We extracted a spectrum for each channel from continuum-subtracted spectral cubes within a 60″ aperture centered on the source (Figure 2). The extraction was performed by using `aperture_photometry()` from `photutils` (L. Bradley 2023) at each wavelength. The continuum subtraction used the image derived from the method described in Section 3.1 and deduced the continuum from each wavelength of the corresponding spectral cube. Given the size of the aperture, the extracted spectra at 52 and 63 μm are effectively the spectra of the entire FoV.

We measured the line fluxes by fitting a 1D Gaussian profile to the extracted spectra, within $\pm$300 km s^{-1} of the source velocity. Due to the telluric features mentioned in Section 3.1, we took special care on the line fitting, especially for the [O I] 63 μm line, where the red wing of the line blends with a prominent telluric feature. To minimize the telluric contamination, we only fit the spectrum from $-$300 to 50 km s^{-1}. The telluric feature at $\lesssim -500$ km s^{-1} is sufficiently separated from the [O III] 52 μm line so that no additional treatment is required for the line fitting.

The fitted line fluxes are listed in Table 2. The fitted line widths and the intrinsic line widths after deconvolving from the instrumental spectral resolution are shown in Figure 2. We note that the [O I] 63 μm line profile is likely to have narrow self-absorption, leading to an underestimation of its line flux when the absorption is not resolved (A. Karska et al. 2014; S. Leurini et al. 2015).

Table 1
Background-subtracted Continuum Fluxes (in Jy) for Each Bandpass Observed with FIFI-LS

[O III] 52 μm	[O I] 63 μm	[O I] 145 μm	CO 186 μm
1244.8 $\pm$ 53	1494.0 $\pm$ 42	1110.1 $\pm$ 24	1054.6 $\pm$ 29

Figure 4 shows the distribution of line emission split into blue- and redshifted velocities compared to the continuum at the same wavelength. To investigate the kinematics of [O III], [O I], and CO, we chose the velocity ranges to avoid telluric features as well as a central exclusion zone of $\pm\zeta$ km s^{-1}, where we define ζ to be equivalent to one-sixth of the velocity resolution of FIFI-LS at the given bandpass. This ensures that any distribution of blue- or redshifted emission is highlighted clearly and is not blurred by instrumental resolution. The blue-and redshifted emission are clearly separated for [O III] 52 μm (despite the poor spectral resolution in this bandpass), while the separation for [O I] 63 μm is notable but less significant. The [O I] 145 μm and CO 186 μm lines show no obvious morphological differences between the blue- and redshifted emission.

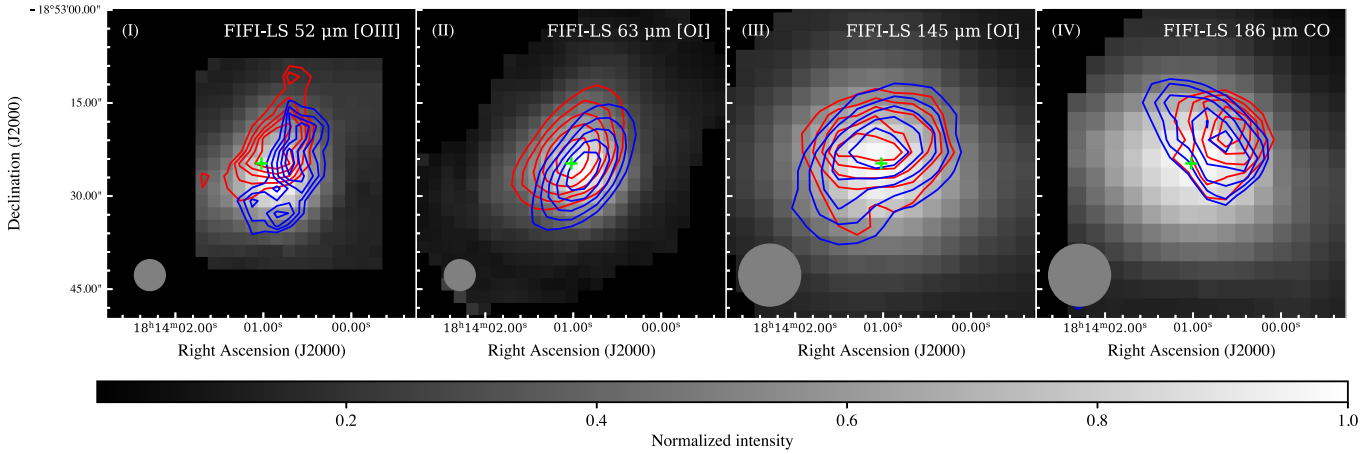

Figure 4. Blue- and redshifted emission of [O III] $^3P_2 \rightarrow {}^3P_1$ at 51.81 μm, [O I] $^3P_2 \rightarrow {}^3P_1$ and $^3P_1 \rightarrow {}^3P_0$ at 63.18 and 145.5 μm, and the CO $J = 14 \rightarrow 13$ line at 185.99 μm. The velocity ranges are $\pm$(50–300) km s^{-1} for every contour map shown. Contours are shown from 50% to 100% with an increment of 10% of the integrated flux for both blue- and redshifted velocities, independently. The background images show the normalized continuum at the corresponding wavelengths. The beam size is shown at the bottom left corner of each panel.

Table 2
Line Fluxes (in Jy km s^{-1}) Obtained via 1D Gaussian Fitting of the FIFI-LS Spectra

[O III] 52 μm	[O I] 63 μm	[O I] 145 μm	CO 186 μm
$7.72 \pm 0.45 \times 10^4$	$7.27 \pm 1.4 \times 10^5$	$3.24 \pm 0.11 \times 10^5$	$3.55 \pm 0.59 \times 10^4$

Table 3
Best-fitting Values of Protostellar Parameters Obtained via SED Fitting

$m_\star$ ($M_\odot$)	M_c ($M_\odot$)	$\dot{m}_\star$ ($M_\odot$ yr^{-1})	$L_{\rm bol}$ ($L_\odot$)	R_c (pc)	A_V (mag)	$\theta_{\rm view}$ (deg)	$\Sigma_{\rm cl}$ (g cm^{-2})
22.4^{+21}_{-11}	223.1^{+92}_{-65}	$9.1^{+5}_{-3} \times 10^{-4}$	$1.6^{+3}_{-1} \times 10^5$	$0.083^{+0.04}_{-0.02}$	287.7 ± 71.5	17.3 ± 8.8	$1.74^{+1.4}_{-0.77}$

4. Analysis

4.1. Protostellar Properties from SED Fitting

Here we discuss properties of the protostar that can be inferred from its SED. In a series of papers (Y. Zhang & J. C. Tan 2011, 2018; Y. Zhang et al. 2013, 2014) a self-consistent model grid of massive protostellar cores has been developed, combining the evolution of the protostar and outflow. This model grid, based on the turbulent core accretion (TCA) model (C. F. McKee & J. C. Tan 2002, 2003), describes the protostellar structures using five parameters, m_*, M_c, $\Sigma_{\rm cl}$, $\theta_{\rm view}$, and A_V, which are the current protostellar mass, the initial core mass, the mean mass surface density of the surrounding clump, the angle of the line of sight to the outflow axis, and the foreground visual extinction. This model grid allows us to constrain the protostellar properties by fitting the SED of G11.94, using the fitting tool `SEDFitter` within the Python package `sedcreator` (R. Fedriani et al. 2023).

We constructed the SED using the extracted continuum fluxes that include both FIFI-LS data and archival measurements (see Section 3.1). We followed the same approach in R. Fedriani et al. (2023) to treat the continuum fluxes at $\leqslant 8$ μm as upper limits, because the model grid does not include polycyclic aromatic hydrocarbon (PAH) features, nor single-photon transient heating effects on small dust grains (J. M. De Buizer et al. 2017; Y. Zhang & J. C. Tan 2018). Both processes could increase the fluxes at $\leqslant 8$ μm. As mentioned in Section 3.1, FIFI-LS continuum measurements at 52 and 63 μm were treated as upper limits due to the possible overestimation of the flux from the interpolation using the Herschel 70 μm image.

Utilizing criteria from R. Fedriani et al. (2023) for establishing which SED fit models are "good," we selected the 44 models with the lowest χ^2 values, ranging from 0.85 to 1.97, i.e., only models with χ^2 less than 2 were considered. In addition, for physical self-consistency, models were required to have an initial core radius, R_c, less than twice the aperture radius (see discussion by R. Fedriani et al. 2023). This is to ensure that the modeled radius does not exceed the extent of emission as seen in the 37 μm FORCAST imaging used to derive the aperture. For explicit details on which models are considered "good," please refer to R. Fedriani et al. (2023). We averaged across all these "good" models to retrieve estimates for protostellar properties (Table 3).

4.2. Origins of Ionized and Atomic Emission

The detection of the [O III] $^3P_2 \rightarrow {}^3P_1$ line ($E_u = 440.5$ K) implies the presence of highly ionized gas. The ionization of [O III] requires an energy of 35.12 eV (i.e., from singly ionized oxygen; I. Wenåker 1990; W. C. Martin et al. 1993). If due to photoionization, this requires a stellar spectrum that is able to

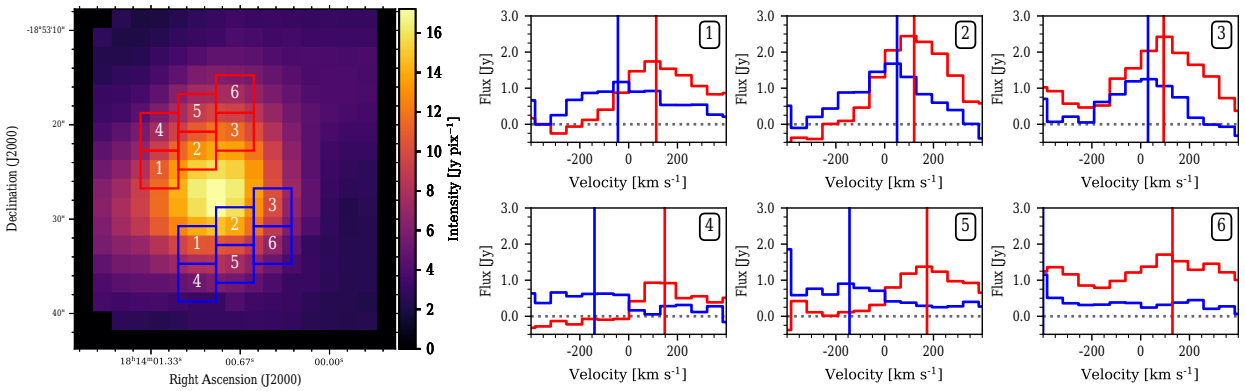

Figure 5. Left: continuum image at 52 μm highlighted with two sets of 2 square pixel apertures in the regions where blue- and redshifted [O III] emission is detected. Right: the continuum-subtracted spectra extracted from the apertures in the left panel. Each panel shows the spectra extracted from a pair of apertures indicated by the number. These pairs of apertures are chosen to be at opposite sides from the source, probing the blue- and redshifted lobes. The peaks of Gaussian profiles fitted from the red and blue wings of the spectra are shown as vertical color-coded bars to highlight the peak velocity of the spectra at both sides of the source, as well as the velocity offset between the two lobes.

fully ionize He to He^+—achieved once photospheric temperatures reach about 37,000 K, which for ZAMS stars is equivalent to approximately an O7 star with a mass of about 30 $M_\odot$ (F. Martins et al. 2005; B. T. Draine 2011). In the context of the TCA model, a protostar of this mass is expected to reach the ZAMS as long as the mass surface density of the clump environment is $\Sigma_{cl} \lesssim 3$ g cm^{-2} (Y. Zhang et al. 2014). It is interesting that these requirements of $m_* \gtrsim 30\,M_\odot$ and $\Sigma_{cl} \lesssim 3$ g cm^{-2} are approximately consistent with those derived from SED modeling, described above.

However, [O III] could also be produced via shock ionization. This is achieved for a fairly narrow range of temperatures at $\sim 9 \times 10^4$ K (e.g., P. Mazzotta et al. 1998; B. T. Draine 2011). Below temperatures of $\sim 6 \times 10^4$ K, most oxygen is in ionization state [O II], while above temperatures of about 1.3×10^5 K, most oxygen is in ionization state [O IV]. Note that postshock temperatures of 0.6, 0.9, and 1.3×10^5 K are achieved for shock speeds of 64, 79, and 95 km s^{-1}, respectively (assuming strong shock jump conditions for mean particle mass $0.636 m_p$, i.e., for singly ionized He, and ignoring effects of magnetic fields).

As discussed in previous sections, the emission of [O III] is kinematically resolved by our FIFI-LS observations (Figure 2). The intrinsic (deconvolved) FWHM of the [O III] line is about 200 km s^{-1}, but with maximum velocities extending to $\pm$400 km s^{-1}. We note that the escape speed from a 30 $M_\odot$ ZAMS star, i.e., with radius of about 8 $R_\odot$, is about 1200 km s^{-1}, which is representative of the maximum terminal velocity of an X-wind (F. H. Shu et al. 2000) or inner disk wind (A. Konigl & R. E. Pudritz 2000). Especially for disk wind models, in which material is launched from a range of radii, there is expected to be a broad range of outflowing gas velocities up to this maximum. If we adopt an observed maximum 3D [O III] outflow velocity limit of 400 km s^{-1}, i.e., assuming a negligible reduction due to inclination effects and deceleration due to the sweeping up of ambient gas, then the fact this is about one-third of the maximum outflow speed expected from a 30 $M_\odot$ ZAMS star may indicate that the innermost region of [O III] outflow launching occurs at $\sim$10 stellar radii. This may imply that the accretion disk is truncated at this location, e.g., by a strong stellar magnetic field, or that the fastest component of the outflow is not well traced by [O III] emission. We also note that the [O I] emission lines appear to be narrower than the [O III] line, i.e., with an FWHM of 46.7 km s^{-1} for the 63 μm line and 86.5 km s^{-1} for the 145 μm line. Their velocities appear to extend to about $\pm$250 km s^{-1}. This indicates the atomic component of the outflow is slower than the ionized one, which is expected if it is launched from larger disk radii and/or suffering from a greater degree of deceleration. Thus, overall, the observed line-of-sight kinematics of [O III] and [O I] appear consistent with the velocity profile expected of a structured ionized–atomic disk wind from a $\sim$20–30 $M_\odot$ protostar that is near the ZAMS, although it is possible that the fastest components are not well traced by our observations.

Examining the morphology of the blue- and redshifted [O III] emission, we see that this shows a clear velocity gradient in the NE–SW direction, which could also indicate a bipolar outflow (Figure 4). In Figure 5, we investigate the peak of the [O III] line emission in the blue- and redshifted areas highlighted by the contours in Figure 4. Each panel in Figure 5 (right) shows the [O III] spectrum at two opposing positions from the source, roughly oriented along the outflow axis. The emission from the redshifted region consistently peaks at a redshifted velocity, and that from the blueshifted region consistently peaks at a blueshifted velocity. We discuss the implications for this velocity gradient in Section 4.5.

In addition, the velocity distribution in the [O I] $^3P_2 \rightarrow {}^3P_1$ line at 63 μm, despite a less prominent separation between the blue- and redshifted velocities, corroborates the velocity gradient seen in the [O III] line. We also expect the morphology of the [O I] 145 μm line ($E_u = 326.6$ K) to be similar to that of the [O III] line. However, the spatial resolution at 145 μm is more than twice as poor as that at 52 and 63 μm, which hinders a confirmation of bipolar outflowing gas using the [O I] 145 μm line. Finally, we note that the CO transition mapped by FIFI-LS appears to trace the innermost region of the protostellar environment, but, in addition to having a line width that is consistent with instrumental broadening, shows no hint of a spatial velocity gradient. The CO emission may therefore trace either a much slower component of the outflow, or gas in the inner infall envelope or accretion disk.

4.3. Additional Outflow Tracers

We have found that the [O III] and [O I] emission observed by SOFIA/FIFI-LS has a plausible origin via photoionization and photodissociation of a disk wind outflow from a massive protostar. Here we consider other evidence for a protostellar outflow from G11.94.

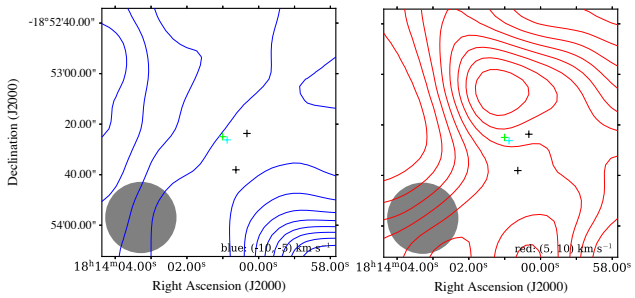

Figure 6. ^{12}CO mapped with the ALMA TP antennas. Note the large beam size (bottom left). The peaks of redshifted (NE) and blueshifted (SW) emission trace the suggested −145° outflow axis.

First, we examine archival ALMA data of G11.94, focusing on the ^{12}CO $J = 2 \rightarrow 1$, ^{13}CO $J = 2 \rightarrow 1$, C^{18}O $J = 2 \rightarrow 1$, H_2CO $3_{03} \rightarrow 2_{02}$, and CH_3OH $4_{22} \rightarrow 3_{12}$ species and transitions, to search for signatures of outflows. Examining ALMA total power (TP) observations of ^{12}CO(2−1) (Figure 6), we see evidence for redshifted emission (i.e., velocities >5 km s^{-1} to the red of v_{lsr}) that peaks to the NE of the source, while equivalently blueshifted emission is to the SW. This axis is consistent with that implied by the [O III] emission, discussed above.

The ^{13}CO, C^{18}O, H_2CO, and CH_3OH ALMA data is available via 12 m and 7 m array observations, which we have combined. The blue and redshifted emission from these tracers is presented in Figure 7. These CO maps also show extended redshifted emission to the NE and blueshifted emission to the SW. However, with the higher angular resolution, we also identify the presence of a hot core 2.″13 to the SW of the G11.94 protostar (marked by a cyan "+" in Figure 7).

From the high-resolution ^{12}CO dataset (Figure 8), we also identify two nearby protostars in the G11.94 field (marked with a black "+" in Figures 1, 7, and 8), one to the W and one to the S. These are detected through the presence of both compact continuum emission and clear bipolar ^{12}CO outflows, with the blueshifted lobe extending to the NNW and the redshifted lobe extending to the SSE in both outflows. The molecular emission from these protostars contaminates the analysis of the outflow morphology from G11.94, particularly in the SW lobe implied from the [O I] and [O III] morphology.

In summary, we detect prominent redshifted emission to the NE of G11.94 in ^{12}CO (both combined 12 m+7 m and TP), ^{13}CO, C^{18}O, H_2CO, and CH_3OH. The ^{12}CO emission in particular possesses relatively high velocities (5–12 km s^{-1}), including several compact spots at ∼10 km s^{-1}. At low velocity ($\lesssim$5 km s^{-1}), the ^{12}CO emission also appears in the NW and SE of G11.94, perpendicular to the inferred outflow direction, likely tracing the gas in the protostellar envelope (Figure 8). To the SW there is clear, collimated blueshifted emission emanating from the continuum peak in both ^{13}CO and C^{18}O, and such a morphology is consistent with the emission of H_2CO and CH_3OH. In the latter two tracers, it is possible that some of the blueshifted emission is due to the nearby protostar, although no corresponding redshifted emission is detected. We therefore associate it with an outflow from G11.94 given its coincident spatial correspondence with emission in ^{13}CO and C^{18}O. This blueshifted emission is not clearly detected in the combined 12 m+7 m ^{12}CO data, but is evident in the ^{12}CO TP image.

Interestingly, in the high-resolution ^{12}CO data, there is a narrow, high-velocity, redshifted filament extending to the SW. The nature of this filament is puzzling, as it extends in the same direction as the inferred blueshifted outflow from FIFI-LS, as well as the ^{13}CO and C^{18}O lines, and in the opposite direction to the higher-velocity redshifted emission seen across all CO isotopologues. There is a velocity gradient in this filament: the emission increases in velocity with distance from either G11.94 or the hot core candidate. This filamentary structure may be interacting with the outflow from the nearby protostar to the NW, as suggested by the overlapping ^{12}CO emission. We also see greater emission of H_2CO and CH_3OH near the overlapped ^{12}CO emission. Further analysis is required to fully understand the nature of this filament, as well as its possible interaction with another protostellar outflow.

Finally, we examine the NIR data obtained with the LBT for Brγ and H_2 lines and *K*-band continuum. A red, green, and blue (RGB) image of these three images is presented in Figure 9. These LBT data reveal a large knot of H_2 emission (red in Figure 9) approximately 1.′5 to the SW of G11.94, along with two smaller knots of emission to the SE and extended faint H_2 emission to the NW. Brγ emission largely traces the emission structures observed in the NIR and MIR (see Figure 1). We also note the presence of a dust lane, oriented on an approximately N–S axis, which bisects and obscures part of the region immediately to the E of the source.

4.4. Discussion on Outflow Orientation

While the [O I] and [O III] emission may hint at a simple outflow morphology, the ALMA data depict a more complex picture. There has yet to be a comprehensive census of the outflow morphology of this region. An outflow from G11.94 is already implied by the broad [Ne II] and ^{12}CO line width (D. S. Shepherd & E. Churchwell 1996; Q.-F. Zhu et al. 2008), and this is confirmed via the detection of broad [O III] and [O I] lines presented in this work. Here we discuss two proposed scenarios for the nature of the outflow from G11.94.

From the observations of FIFI-LS and ALMA, an outflow axis that is oriented in a NE–SW direction is implied, with the red lobe extending to the NE and the blue lobe extending to the SW. The morphology of [O I], [O III], and CO isotopologues indicates a wide-angle outflow, especially in the NE lobe. While the blueshifted SW lobe is not clearly seen in ^{12}CO, except for the channels between (−6, −2) km s^{-1} (Figure 8), possibly due to confusion with quiescent gas, the blueshifted lobe can be traced by the ^{13}CO and C^{18}O lines, which trace denser gas, as well as the emission of methanol and formaldehyde (Figure 7). We estimate a ∼100°–110° edge-to-edge outflow opening angle of the redshifted lobe. Such a large outflow opening angle can result in a flattened structure which appears to be perpendicular to the outflow direction (Y. Zhang et al. 2014), similar to the morphology of the low-velocity ^{12}CO emission. This could explain some of the perpendicularly elongated MIR and NIR emission features seen in Figures 1 and 9, respectively. The blueshifted lobe appears to have a narrower opening angle than the redshifted lobe. The large H_2 knot to the SW detected by the LBT (Figure 9) is aligned well with the blueshifted outflow axis suggested by this interpretation.

It is expected that massive protostars begin to ionize their surroundings in the later stages of their evolution as they

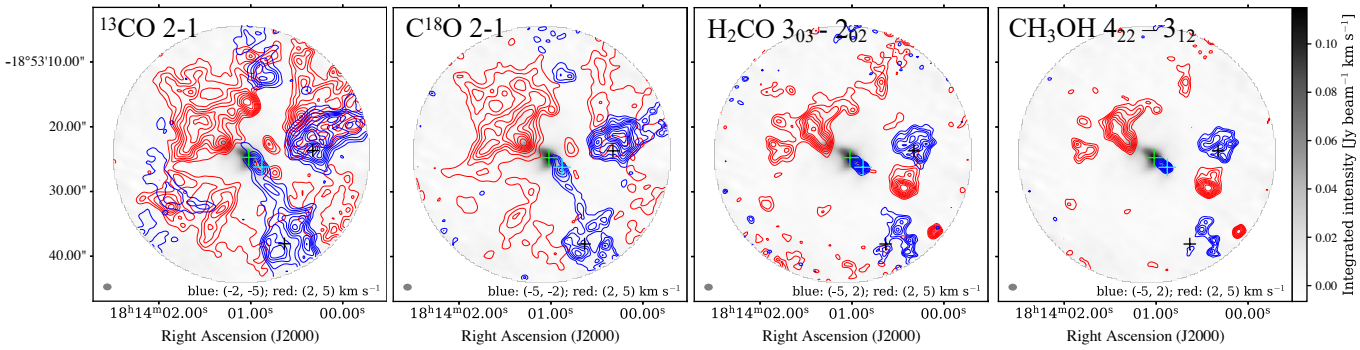

Figure 7. Maps of the ^{13}CO $J = 2 \rightarrow 1$, C^{18}O $J = 2 \rightarrow 1$, H_2CO $3_{03} \rightarrow 2_{02}$, and CH_3OH $4_{22} \rightarrow 3_{12}$ lines as observed by ALMA. The contours show the line emission in the velocity ranges indicated in the legends, while the images show the continuum emission at 218.935 GHz. The corresponding beam sizes are shown at the bottom left corner of each panel. The emission at the inner ± 2 km s^{-1} is excluded to avoid the kinematically quiescent gas close to the source velocity. The green "+" marks the ALMA continuum peak, while the cyan "+" marks the location of a hot core candidate to the SW of the source. Two protostars in the field are marked with a black "+".

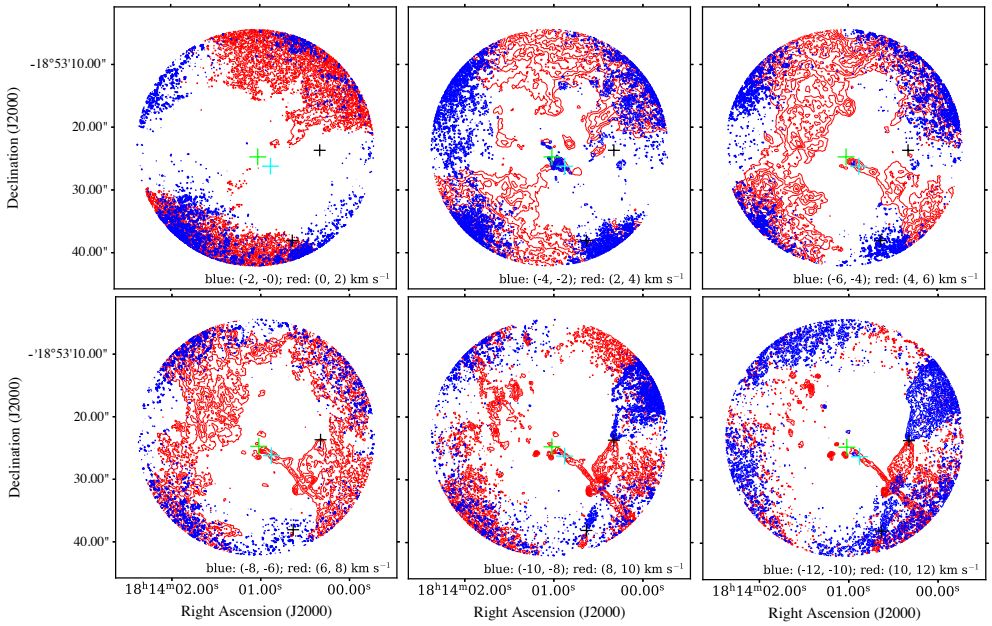

Figure 8. Channel maps of ^{12}CO emission in 2 km s^{-1} intervals at both the red- and blueshifted velocities. The green "+" marks the ALMA continuum peak, while the cyan "+" marks the location of a hot core candidate to the SW of the source. The two protostars in the field (black "+") can both be seen driving outflows with both blue lobes to the NNE and both red lobes to the SSW. The peculiar redshifted filament emanating from G11.94 extending to the SW can be seen above 6 km s^{-1}, in the same direction as the blueshifted [O III] and [O I] emission detected with FIFI-LS.

contract toward the ZAMS. Moreover, the outflow opening angle is expected to widen significantly as protostars evolve (e.g., H. Beuther & D. Shepherd 2005; H. G. Arce et al. 2007; J. C. Tan et al. 2014). Thus, a region with ionized emission could also possess a wide-angle outflow. The presence of [O III] emission in G11.94, together with the morphology of molecular lines observed with ALMA, supports this scenario.

However, there are some issues with the interpretation of a NE–SW outflow. Both the NIR continuum observed with Spitzer IRAC bands and the Brα line imaged by the LBT show extended emission in the NW–SE direction, perpendicular to the NE–SW outflow discussed in previous paragraphs. This emission in the NW–SE direction could be an outflow. However, there are several reasons why we favor the outflow in the NE–SW direction instead of this scenario. First, the morphology of the NIR continuum and the Brα line does not necessarily contradict the NE–SW outflow axis. In the outflow with a wide opening angle, the NIR radiation can be mostly scattered off a wide cavity, resulting in emission elongated perpendicular to the outflow axis. Another issue with this NW–SE outflow scenario is that only low-velocity ($\lesssim$5 km s^{-1}) ^{12}CO emission traces gas at the same NW–SE direction, which is toward the edge of the ALMA FoV with no apparent connection to G11.94 or any other continuum sources. Compared to the broad line width in [O I] and [O III], this low-velocity CO emission is unlikely to trace the same material; thus, this does not strongly support the NW–SE outflow scenario.

The faint extended H_2 emission to the NW seen with the LBT may support a NW–SE interpretation. However, closer investigation shows that it may be separated into two components. The W component is consistent with emission from the nearby protostar to the W, and the E component is

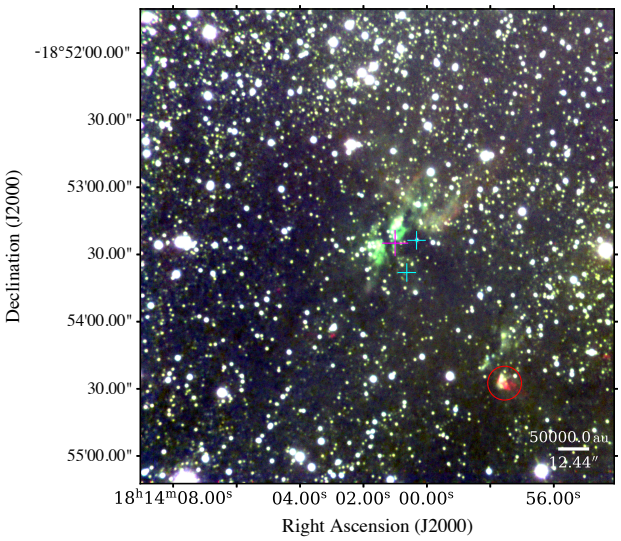

Figure 9. NIR imaging of G11.94 with the LBT. Red channel is H_2, green is Brγ, and blue is *K*-band continuum. The source is identified with a magenta cross, and nearby protostars are shown with cyan. The red circle highlights a large H_2 knot approximately 1.′5 to the SW of G11.94.

consistent with a cavity wall from a wide-angle outflow emanating from G11.94.

One feature that the NE–SW outflow, traced by [O I] and [O III], cannot explain is the high-velocity redshifted filament at the SW of G11.94 seen in ^{12}CO. We speculate that this filament may be a jet from the hot core candidate.

In summary, we conclude that the most likely scenario is that the [O I] and [O III] emission is tracing an outflow in the NE–SW direction, corroborated by the emission of CO isotopologues, methanol, and formaldehyde. This outflow is poorly collimated with a wide opening angle. The redshifted lobe faces the NE, while the blueshifted lobe faces the SW. This scenario is the most consistent with an evolved protostar driving the ionization at the base of its outflow cavity.

4.5. Outflow Orientation from FIFI-LS Data

The FIFI-LS continuum and line emission morphology provide three independent measurements of the outflow axis orientation. The P.A. can be determined from [O III] and [O I] $^3P_2 \rightarrow {}^3P_1$ at 63 μm emission ($PA_{[O\ III]}$ and $PA_{[O\ I]}$). As a result of the relatively low spatial resolution, the emission features can be approximated as 2D Gaussians. We fit the 2D Gaussian peak positions of the blue- and redshifted emission and measured the P.A. from these two positions. The $PA_{[O\ III]}$ is $-144.^\circ0 \pm 15.^\circ0$ and the $PA_{[O\ I]}$ is $-141.^\circ7 \pm 11.^\circ2$.

We can also measure the continuum peak offsets from the red to the blue channel of FIFI-LS. The PA_{cont} discussed in Section 3.1, $-126.^\circ2 \pm 12.^\circ4$ and $-88.^\circ5 \pm 19.^\circ3$, are the two measurements (from 52 and 63 μm, respectively) for the direction of the blueshifted lobe. However, given the small magnitude of the offset for the latter measurement ($1.''0 \pm 0.''3$), we should treat the first measurement (with an offset of $2.''5 \pm 0.''5$) as more robust. The agreement between the P.A. calculated from FIFI-LS [O I] and [O III] emission indicates that the P.A. for this suggested outflow is $\sim -142°$. Furthermore, the P.A. derived from oxygen lines is consistent with the P.A. calculated for the relative offset between 52 and 186 μm continuum imaging.

4.6. Mass and Momentum Outflow Rates

4.6.1. The Ionized Outflow

Using the flux of the [O III] line in G11.94, we attempt to infer the oxygen column density and place limits on the outflow rates of the ionized outflow. We relate the line luminosity of [O III] at 52 μm to the gas mass traced by [O III]. First, the line luminosity can be expressed as a volume integral:

$$L_{[O\ III]} = \int_V f_V\, n_e n(O^{2+}) j_{[O\ III]}(n_e, T_e) dV, \tag{1}$$

where f_V is the volume filling factor, $n(O^{2+})$ is the density of ionized oxygen, and $j_{[O\ III]}(n_e, T_e)$ is the emissivity of the [O III] 52 μm line, which is a function of electron density (n_e) and electron temperature (T_e). We assume that within the ionized region, which is treated as distinct from the atomic part of the outflow traced by [O I], all O is in the O^{2+} ionization state and adopt an O abundance of $X_O = 3 \times 10^{-4}$ with respect to H nuclei. Within the ionized region we also assume that He is singly ionized, so that $n_e = 1.1 n_H$. Then the 52 μm line flux can be expressed as

$$F_{[O\ III]} = \frac{L_{[O\ III]}}{4\pi d^2} = \frac{f_V V}{1.1} \langle n_e^2 \rangle X_O \frac{j_{[O\ III]}(n_e, T_e)}{4\pi d^2}, \tag{2}$$

where d is the distance to the source.

The average oxygen column density can be evaluated via a volume integral as

$$N_O = \frac{1}{\Omega_{aper} d^2} \int_V f_V\, n_O dV = f_V X_O \frac{\langle n_e \rangle V}{1.1 \Omega_{aper} d^2}, \tag{3}$$

where Ω_{aper} is the solid angle of the aperture. If we assume a uniform distribution so that $\langle n_e^2 \rangle = \langle n_e \rangle^2$ and combine Equations (2) and (3), we obtain

$$F_{[O\ III]} = N_O \frac{\Omega_{aper}}{4\pi} \langle n_e \rangle j_{[O\ III]}(n_e, T_e), \tag{4}$$

$$= N_H X_O \frac{\Omega_{aper}}{4\pi} \langle n_e \rangle j_{[O\ III]}(n_e, T_e), \tag{5}$$

where N_O and N_H are the column densities of O and H nuclei that are associated with the [O III] emitting, i.e., ionized, region.

Using `PyNeb` (V. Luridiana et al. 2015), we calculate the emissivity of [O III] at given values of n_e and T_e and thus link the observed flux of the [O III] line to the column of the ionized gas. Figure 10 shows example model results for cases with $n_e = 100$ and 1000 cm^{-3}, both with $T_e = 10^4$ K, with the extent of the ionized region guided by the observed size of [O III] emission from G11.94, i.e., a radial extent of 10″, equivalent to $R_{out} = 0.2$ pc (or 40,000 au). We see below that these values of density are representative of self-consistent solutions for the emission from an ionized outflow from G11.94.

When comparing to the observed [O III] flux, we need to consider the impact of dust extinction. As a fiducial value for the mass surface density of the extincting material, we adopt 50% of that of the clump environment, i.e., $\Sigma = \Sigma_{cl}/2 = 0.87$ g cm^{-2}, which is representative of the value inferred from SED model fitting. The value of the opacity at 52 μm depends on the adopted dust model. For the dust model of S.-H. Kim et al. (1994), i.e., the dust model used in the radiative transfer

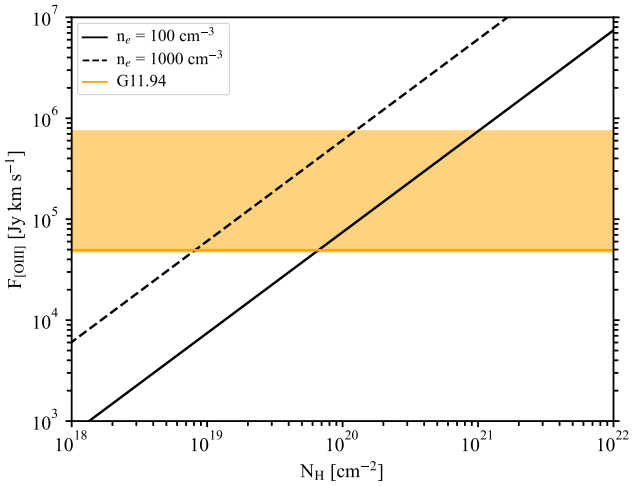

Figure 10. Expected flux of [O III] 52 μm as a function of column density of H nuclei in the ionized region, which is assumed to extend over a 10″ radius aperture, based on PyNeb models for a temperature of 10^4 K and densities of $n_e = 100\,\mathrm{cm}^{-3}$ (black solid line) and $1000\,\mathrm{cm}^{-3}$ (black dashed line). The observed flux from G11.94 is shown by the horizontal yellow line. The horizontal shaded band shows a range of flux values extending upward by a factor of 14.9 that accounts for potential effects of dust extinction (see text).

simulations of Y. Zhang & J. C. Tan (2018), the value of κ at 52 μm is $1.084\,\mathrm{cm}^2\,\mathrm{g}^{-1}$ (note: per gram of gas). However, for the moderately coagulated thin ice mantle model of V. Ossenkopf & T. Henning (1994) (hereafter the OH5 dust model), the equivalent κ is $3.09\,\mathrm{cm}^2\,\mathrm{g}^{-1}$ (per gram of gas). Therefore we consider that the optical depth of the foreground material could be in the range $\tau = \kappa\Sigma \simeq 0.9$–2.7 so that the intrinsic flux of [O III] emission may be 2.5 to 14.9 times greater than the observed value. Given these considerations, in Figure 10 we show a range of values for the [O III] flux from G11.94, from the observed value of $\sim 5 \times 10^4\,\mathrm{Jy\,km\,s}^{-1}$ up to $2.3 \times 10^5\,\mathrm{Jy\,km\,s}^{-1}$, and adopt a fiducial value of $1 \times 10^5\,\mathrm{Jy\,km\,s}^{-1}$.

With the above results, we estimate that the average column density of the ionized outflow is $N_\mathrm{H} \sim 2 \times 10^{19}\,\mathrm{cm}^{-2}$ for the case with $n_e = 1000\,\mathrm{cm}^{-3}$ and $2 \times 10^{20}\,\mathrm{cm}^{-2}$ for the case with $n_e = 100\,\mathrm{cm}^{-3}$. Given the morphology of the [O III] emission we expect a volume filling factor of order unity and thus adopt $f_V = 1/3$ in a spherical volume of 10″ radius. This implies a gas density in the ionized outflow of $n_\mathrm{H} = 3N_\mathrm{H}/(4f_V R_\mathrm{out}) \rightarrow 75$ and $750\,\mathrm{cm}^{-3}$. Thus, approximately self-consistent results are achieved for the case $n_e = 300\,\mathrm{cm}^{-3}$, which implies $N_\mathrm{H} \simeq 8.7 \times 10^{19}\,\mathrm{cm}^{-2}$ and $n_\mathrm{H} \simeq 325\,\mathrm{cm}^{-3}$, i.e., $n_e \simeq 360\,\mathrm{cm}^{-3}$.

With this value of $n_\mathrm{H} = 325\,\mathrm{cm}^{-3}$ or $N_\mathrm{H} = 8.7 \times 10^{19}\,\mathrm{cm}^{-2}$, we estimate a mass of the ionized outflow of $M_\mathrm{out,O\,III} = 0.12\,M_\odot$ that is present within a 0.2 pc radius of the source. To calculate the mass flux in this component of the outflow, we estimate the timescale for the outflow to cross this region, i.e., to flow from the protostar to a radial distance of 0.2 pc. For this, we adopt an outflow speed of $v_\mathrm{out,O\,III} = 200\,\mathrm{km\,s}^{-1}$, i.e., the observed half-width at half-maximum (HWHM) of the [O III] emission at 52 μm with FIFI-LS. Given the uncertainty in the orientation of the source, for simplicity we assume this is representative of the 3D speed of the outflow. Thus the outflow timescale is $t_\mathrm{out} = R_\mathrm{out}/v_\mathrm{out} = 980\,\mathrm{yr}$. Thus the mass flux in the [O III]-traced outflow is $1.2 \times 10^{-4}\,M_\odot\,\mathrm{yr}^{-1}$. Similarly, the total momentum in the ionized component of the outflow is $p_\mathrm{out,O\,III} = m_\mathrm{out,O\,III} v_\mathrm{out,O\,III} = 16\,M_\odot\,\mathrm{km\,s}^{-1}$ and the momentum outflow rate is $\dot{p}_\mathrm{out,O\,III} = 0.025\,M_\odot\,\mathrm{km\,s}^{-1}\,\mathrm{yr}^{-1}$. These results are listed in Table 4.

We note that the protostellar accretion rate estimated from SED fitting has a value of $\sim 9 \times 10^{-4}\,M_\odot\,\mathrm{yr}^{-1}$. The primary outflow is thus expected to have a mass injection rate of about 10% of this (e.g., Y. Zhang & J. C. Tan 2018), i.e., $\sim 9 \times 10^{-5}\,M_\odot\,\mathrm{yr}^{-1}$. We see that the ionized component of the outflow has a mass flux that is very similar to that expected for the total primary outflow.

We also note that [O III] emission from massive protostars is relatively rare, with G11.94 being one of the few SOMA Atomic Outflow Survey sources that show such strong emission. Recently, A. Karska et al. (2025) have reported [O III] emission from the massive protostar DR21 Main, with their setup including both the 52 and 88 μm lines. These authors also used PyNeb to infer conditions in the ionized gas, deriving $T_e \sim 8000$ K and $n_e \sim 250\,\mathrm{cm}^{-3}$, i.e., similar densities to those we have inferred.

4.6.2. The Atomic Outflow

We model the [O I] line intensities and line ratios to estimate the column density of material associated with this emission and therefore the mass and momentum flux of this "atomic" component of the G11.94 outflow. However, the [O I] 63 μm line is known to have self-absorption at the line center (S. Leurini et al. 2015). Thus, simply dividing the peak intensity of the two [O I] lines is unlikely to provide a realistic measurement of the line ratio. To avoid the absorption-contaminated line center, we estimate the line ratio on the wings of these two lines, although the 63 μm [O I] fit is further hindered by the large telluric feature on the red side of the spectrum. The two [O I] lines were observed with different instrumental spectral resolution (Section 2.1). We first convolve the [O I] 63 μm spectrum to match the spectral resolution at 145 μm. Then, we divide the spectra of the 63 μm over the [O I] 145 μm and take the average across -300 to $-100\,\mathrm{km\,s}^{-1}$, exclusively on the blue portions of the spectra. The measured ratio is 2.30 ± 0.20.

However, again, dust extinction is another factor that may affect the relative intensity of the [O I] 63 and 145 μm lines. Specifically, the higher opacity at 63 μm preferentially lowers the luminosity of the [O I] 63 μm line. The S.-H. Kim et al. (1994) dust model κ values at 63 and 145 μm are 0.735 and $0.133\,\mathrm{cm}^2\,\mathrm{g}^{-1}$, respectively. If the OH5 dust model is used, then these values would be 2.09 and $0.47\,\mathrm{cm}^2\,\mathrm{g}^{-1}$, respectively. The ratio of the [O I] line intensities is affected by extinction via

$$\frac{I_{63,\mathrm{obs}}}{I_{145,\mathrm{obs}}} = \frac{I_{63,\mathrm{true}} e^{-\tau_{63}}}{I_{145,\mathrm{true}} e^{-\tau_{145}}} = \frac{I_{63,\mathrm{true}}}{I_{145,\mathrm{true}}} e^{-(\Delta\kappa_{63-145}\Sigma)}, \quad (6)$$

where $\Delta\kappa_{63-145} = \kappa_{63\mu\mathrm{m}} - \kappa_{145\mu\mathrm{m}}$. Again we adopt an extincting mass surface density of $\Sigma = \Sigma_\mathrm{cl}/2 = 0.87\,\mathrm{g\,cm}^{-2}$. Under such conditions, $e^{-(\Delta\kappa_{63-145}\Sigma)} = 0.59$ for the S.-H. Kim et al. (1994) dust model and 0.24 for the OH5 dust model. Given these considerations, we consider a range of values of line intensity ratios from 2.3 to 9.6.

For our modeling of expected line ratios and intensities, we utilize a 1D adaptation of the 3D-PDR software (T. G. Bisbas et al. 2012), considering a range of uniform densities, $\log(n_\mathrm{H}/\mathrm{cm}^{-3}) = 2, 3, 4, 5$, and a range of UV flux densities, $\log(\chi/\chi_0) = 1, 3, 5$ (normalized to the radiation field

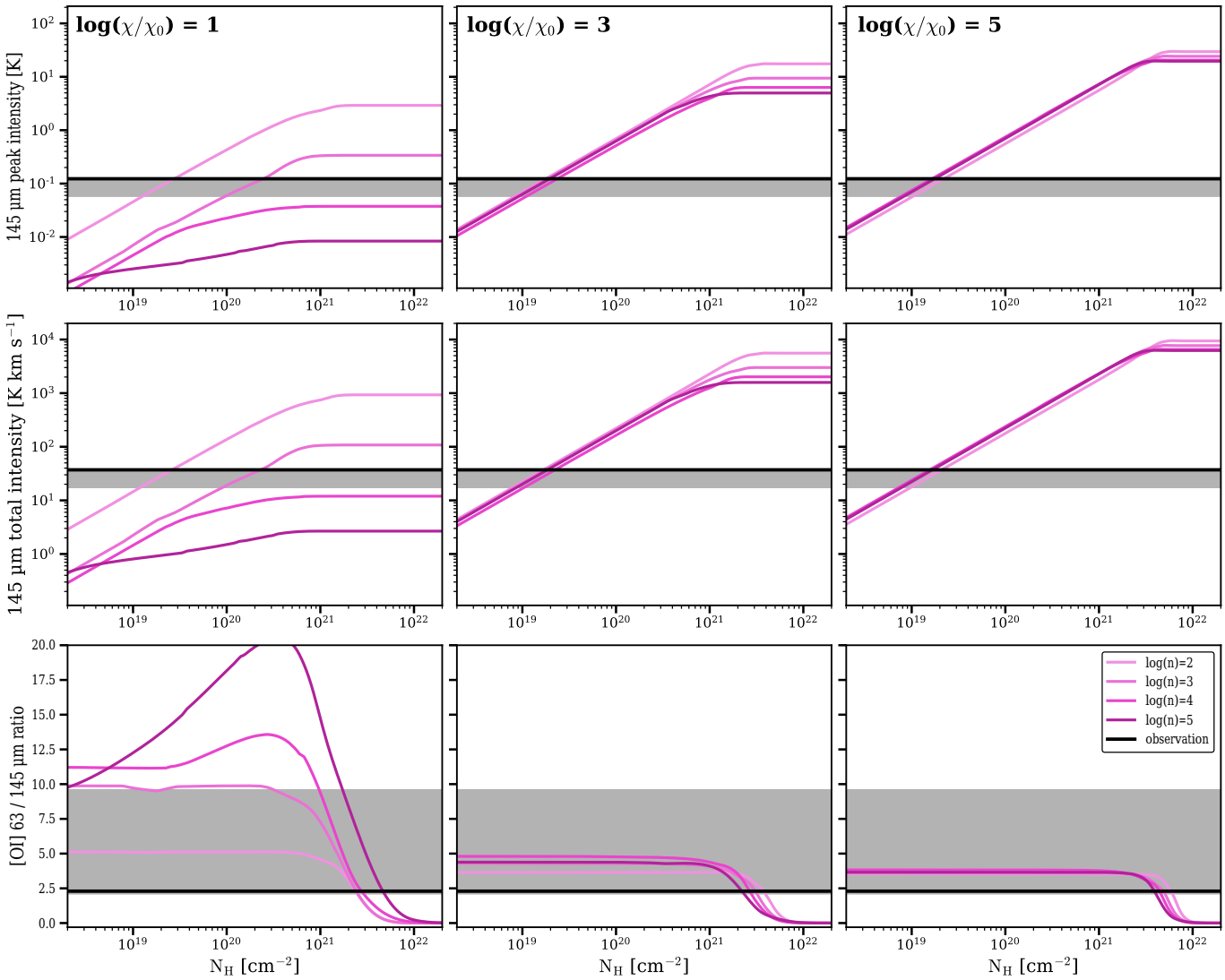

Figure 11. 3D-PDR modeling to predict [O I] emission properties from total gas column density, N_H, for a range of FUV flux densities (columns) and a range of environment densities (see legend). From top to bottom, gas column density is plotted against [O I] 145 μm peak intensity, [O I] 145 μm total intensity, and [O I] 63/145 μm ratio. Uncertainties are derived from combining the uncertainty from flux measurements (negligible in rows 1 and 2) with the range of possible dust extinction, which dominates the uncertainty in all plots. The flux ratio measurement in the third row is more uncertain because the ratio is calculated from a line wing fit.

Table 4
Ionized, Atomic, and Molecular Outflow Properties of the Massive Protostar G11.94

	m_{out} ($M_\odot$)	v_{out} (km s^{-1})	p_{out} ($M_\odot$ km s^{-1})	t_{out} (yr)	$\dot{m}_w$ ($M_\odot$ yr^{-1})	$\dot{p}_w$ ($M_\odot$ km s^{-1} yr^{-1})
Ionized	0.116	211	24.5	980	1.2×10^{-4}	2.5×10^{-2}
Atomic	0.038	43.3	1.65	7500	5.1×10^{-6}	2.2×10^{-4}
Molecular	4.14	25.9	107	15,700	2.6×10^{-4}	6.8×10^{-3}

of B. T. Draine 1978). We assume a constant cosmic-ray ionization rate of 10^{-16} s^{-1} (A. Dalgarno 2006; B. A. L. Gaches et al. 2022), solar metallicity composition, and "turbulent" (i.e., kinematic) broadening of 100 km s^{-1}, which is designed to reflect the velocity distribution of the outflow. We model the [O I] fluxes at 63 and 145 μm in each simulated PDR by solving the respective radiative transfer equation (T. G. Bisbas et al. 2017).

To obtain an estimate for the total column density of H nuclei, N_H, we use three metrics: the peak intensity of the 145 μm line ($I_{145,peak}$); the total flux of the 145 μm line (F_{145}); and the ratio of the 63 to 145 μm line intensities (I_{63}/I_{145}). We note that the peak intensity is impacted by the instrumental resolution and we convolve the model with the appropriate value at each wavelength. From the results shown in Figure 11 we conclude that for the higher FUV field cases that we consider to be the

most relevant, values of $N_{\rm H} \simeq 2 \times 10^{19}\,{\rm cm}^{-2}$ are favored. Given the uncertainties in the line ratio induced by potential effects of differential extinction, this ratio provides little constraint on the volume density of the gas.

Following the methodology from Section 4.6.1 and adopting a radius of 17″ for the extent of the [O I] outflow, (68,000 au, $R_{\rm out,O\,I} = 0.33$ pc), the mass in the [O I] outflow is estimated to be $m_{\rm out,O\,I} = 0.038\,M_\odot$. To calculate the mass flux in this component of the outflow we estimate the outflow crossing timescale, i.e., the flow from the protostar to a radial distance of 0.33 pc. For this we adopt a line-of-sight outflow speed of 43.3 km s^{-1}, i.e., the observed HWHM of the [O I] emission at 145 μm. As for the ionized outflow traced by [O III], we also assume that the intrinsic 3D velocity is well represented by this value. Thus the outflow timescale is $t_{\rm out,O\,I} = R_{\rm out,O\,I}/v_{\rm out,O\,I} = 7500$ yr and the implied mass flux is $\dot{m}_{\rm out,O\,I} = 5.1 \times 10^{-6}\,M_\odot\,{\rm yr}^{-1}$. The momentum in the observed outflow aperture is estimated to be $p_{\rm out,O\,I} = m_{\rm out,O\,I} v_{\rm out,O\,I} = 1.6\,M_\odot\,{\rm km\,s}^{-1}$ and the momentum outflow rate is $\dot{p}_{\rm out,O\,I} = 2.2 \times 10^{-4}\,M_\odot\,{\rm km\,s}^{-1}\,{\rm yr}^{-1}$.

Comparing again to the protostellar accretion rate estimated from SED fitting, which has a value of $\sim 9 \times 10^{-4}\,M_\odot\,{\rm yr}^{-1}$, and thus to the expected primary outflow mass injection rate of $\sim 9 \times 10^{-5}\,M_\odot\,{\rm yr}^{-1}$, we see that the atomic component of the outflow is $\lesssim$10% of the expected total mass flux of the primary outflow.

4.6.3. The Molecular Outflow

To estimate the mass outflow rate of the molecular outflow, we utilize the ALMA TP observations of the ^{12}CO 2 → 1 line, which have an angular resolution (half-power beamwidth) of 22.″6. We extract a spectrum from a beam area centered on the protostar, with a radial extent of 22.″6, i.e., 90,000 au, or 0.44 pc. Utilizing methodology from M. M. Dunham et al. (2014) and Y. Zhang et al. (2019), we derive the outflow mass and momentum from the TP spectral cube, excluding the inner ±5 km s^{-1} to avoid confusion with any surrounding quiescent gas. We assume optically thin emission, a ^{12}CO abundance of 10^{-4} with respect to H_2 (M. A. Frerking et al. 1982; J. H. Lacy et al. 1994; J. Hatchell et al. 2007), and an excitation temperature $T_{\rm ex}$ for the ^{12}CO (2 → 1) transition of 17.5 K. This temperature provides the minimum estimate for outflow mass. Picking a $T_{\rm ex}$ of 50.0 K, which is generally the upper limit for mass estimates using low-J CO transitions, would increase our estimates for mass by a factor of 1.5. We calculate the outflow mass in each velocity channel and then sum over the spectrum to obtain a total CO-traced outflow mass of $m_{\rm out,mol} = 4.14\,M_\odot$. We evaluate the mass-weighted mean line-of-sight velocity to be 25.9 km s^{-1} and again assume this to be representative of the 3D velocity. The total momentum is then estimated to be 107 $M_\odot$ km s^{-1}. The outflow timescale is $t_{\rm out,mol} = R_{\rm out,mol}/v_{\rm out,mol} = 15{,}700$ yr. Thus the mass and momentum fluxes in the molecular outflow are $\dot{m}_{\rm out,mol} = 2.6 \times 10^{-4}\,M_\odot\,{\rm yr}^{-1}$ and $\dot{p}_{\rm out,mol} = 6.8 \times 10^{-3}\,M_\odot\,{\rm km\,s}^{-1}\,{\rm yr}^{-1}$.

Comparing to the other components, we see that the molecular outflow appears to dominate the total mass flux, being 3.1 times greater than the ionized component. However, the momentum flux of the molecular outflow is about 2.5 times smaller than that of the ionized component. The atomic outflow is a very minor component in both metrics, between ∼1% and 10% of the values for the molecular and ionized components. These results imply that the ionized outflow dominates the contribution of the total outflow force, albeit with a significant fraction, i.e., ∼30%, being carried by molecular gas. The relatively low velocity of the molecular gas and its comparatively high mass flux rate suggest that it is primarily composed of swept-up gas from the natal core envelope.

5. Conclusions

We have presented first results from the SOMA Atomic Outflow Survey, which has used SOFIA/FIFI-LS to observe a sample of massive protostars, in the [O I] lines at 63 and 145 μm, the ionized [O III] line at 52 μm, and the CO line at 186 μm. Here we have focused on the source G11.94, which presents relatively strong [O III] emission. The main conclusions of our investigation are as follows:

1. The massive protostar G11.94 exhibits strong ionized and atomic oxygen lines with broad line widths: ∼200 km s^{-1} in [O III] and ∼40−80 km s^{-1} in [O I].
2. The kinematic distribution of the [O III] and [O I] emitting gas suggests a bipolar outflow with the red lobe extending to the NE and the blue lobe to the SW. We infer a P.A. for the blueshifted lobe of approximately −143°.
3. This ionized and atomic outflow is corroborated by molecular emission in ALMA observations of ^{12}CO, ^{13}CO, C^{18}O, H_2CO, and CH_3OH. From these observations, it appears that the blueshifted lobe of the molecular outflow is more collimated than the brighter, wide (∼110°) angle redshifted outflow lobe.
4. LBT imaging in the NIR reveals a complicated morphology. One interpretation is that NIR-bright emission traces the base of wide-angle outflow cavities.
5. We have estimated a mass flux of the ionized outflow that is about 10% of the accretion rate derived from SED-fitted TCA models of the protostar. This suggests that the primary outflow, i.e., outflow launched directly from the disk, is dominated by the ionized outflow. This is consistent with our estimates of the momentum flux of the ionized outflow, which dominates over the atomic and molecular components. However, the molecular outflow dominates the total mass flux, suggesting it is mainly composed of swept-up, secondary outflow gas. The atomic outflow is subdominant in both mass and momentum flux compared to the other components.
6. A dominant ionized protostellar outflow is the expected signature of a very massive protostar in the later stages of its growth, i.e., with a protostellar structure that has contracted to near the ZAMS, leading to high rates of H ionizing luminosity. The fact that the outflow is seen in [O III] line emission indicates that a photospheric temperature of at least 37,000 K is required, i.e., to enable the ionization of He to He$^+$, which requires a ZAMS stellar mass of at least ∼30 $M_\odot$. Such a mass is consistent with the results of SED fitting, i.e., $m_* = 22.4^{+21}_{-11} M_\odot$, although this estimate is subject to significant uncertainties. Indeed, the presence of strong [O III] emission places additional constraints on these models, helping to break some of the degeneracy present in SED fitting.
7. Future observations are needed to confirm the above conclusions. In particular, improved kinematic characterization of the protostar is needed, e.g., a dynamical mass estimate from accretion disk tracers using high-resolution ALMA observations. Improved kinematic

characterization of the molecular, atomic, and ionized outflow is also needed, e.g., with ALMA and future far-IR facilities, such as PRIMA.

Acknowledgments

We thank the anonymous referee for helpful comments. We thank the ALMA-ATOMS/QUARKS survey team for providing their fully prepared ^{12}CO data cube. P.O. acknowledges support from a Virginia Initiative on Cosmic Origins (VICO) summer undergraduate fellowship. Y.-L.Y. acknowledges support from a Grant-in-Aid from the Ministry of Education, Culture, Sports, Science, and Technology of Japan (20H05845, 20H05844, 22K20389, and 25H00676), and a pioneering project in RIKEN (Evolution of Matter in the Universe). J.C.T. acknowledges support from ERC Advanced Grant MSTAR (788829) and NSF AAG grant 2206450. T.G.B. acknowledges support from the Leading Innovation and Entrepreneurship Team of Zhejiang Province of China (grant No. 2023R01008). R.F. acknowledges support from the grant PID2023-146295NB-I00, and from the Severo Ochoa grant CEX2021-001131-S funded by MCIN/AEI/10.13039/501100011033 and by "European Union NextGenerationEU/PRTR." Based in part on observations made with the NASA/DLR Stratospheric Observatory for Infrared Astronomy (SOFIA). SOFIA is jointly operated by the Universities Space Research Association, Inc. (USRA), under NASA contract NNA17BF53C, and the Deutsches SOFIA Institut (DSI) under DLR contract 50 OK 2002 to the University of Stuttgart. Additional financial support for this work was provided by NASA through award #09_0169 issued by USRA.

ORCID iDs

Phillip Oakey https://orcid.org/0009-0002-9291-1487
Yao-Lun Yang https://orcid.org/0000-0001-8227-2816
Jonathan C. Tan https://orcid.org/0000-0002-3389-9142
Thomas G. Bisbas https://orcid.org/0000-0003-2733-4580
Rubén Fedriani https://orcid.org/0000-0003-4040-4934
Kei E. I. Tanaka https://orcid.org/0000-0002-6907-0926
Zoie Telkamp https://orcid.org/0000-0001-6465-9590
Yichen Zhang https://orcid.org/0000-0001-7511-0034
Christian Fischer https://orcid.org/0000-0002-7299-8661
Lianis Reyes Rosa https://orcid.org/0000-0002-2986-2304

References

Arce, H. G., Shepherd, D., Gueth, F., et al. 2007, in Protostars and Planets V, ed. B. Reipurth, D. Jewitt, & K. Keil, 245 (Univ. of Arizona Press)
Astropy Collaboration, Price-Whelan, A. M., Lim, P. L., et al. 2022, ApJ, 935, 167
Bally, J. 2016, ARA&A, 54, 491
Becker, R. H., White, R. L., & Helfand, D. J. 1994, ASPC, 61, 165
Beuther, H. 2007, arXiv:0712.1109
Beuther, H., & Shepherd, D. 2005, ASSL, 324, 105
Bisbas, T. G., Bell, T. A., Viti, S., Yates, J., & Barlow, M. J. 2012, MNRAS, 427, 2100
Bisbas, T. G., Tanaka, K. E. I., Tan, J. C., Wu, B., & Nakamura, F. 2017, ApJ, 850, 23
Bradley, L. 2023, astropy/photutils: 1.8.0, v1.8.0, Zenodo, doi:10.5281/zenodo.7946442
CASA Team, Bean, B., Bhatnagar, S., et al. 2022, PASP, 134, 114501
Churchwell, E., Babler, B. L., Meade, M. R., et al. 2009, PASP, 121, 213
Churchwell, E., Walmsley, C. M., & Wood, D. O. S. 1992, A&A, 253, 541
Colditz, S., Beckmann, S., Bryant, A., et al. 2018, JAI, 7, 1840004
Craig, M., Crawford, S., Seifert, M., et al. 2022, astropy/ccdproc: 2.3.1–fixes astropy 5.1 compatibility, v2.3.1, Zenodo, doi:10.5281/zenodo.6533213
Crowther, P. A., & Conti, P. S. 2003, MNRAS, 343, 143
Dalgarno, A. 2006, PNAS, 103, 12269
De Buizer, J. M., Liu, M., Tan, J. C., et al. 2017, ApJ, 843, 33
De Buizer, J. M., Radomski, J. T., Telesco, C. M., & Piña, R. K. 2003, ApJ, 598, 1127
Draine, B. T. 1978, ApJS, 36, 595
Draine, B. T. 2011, Physics of the Interstellar and Intergalactic Medium (Princeton Univ. Press)
Dunham, M. M., Arce, H. G., Mardones, D., et al. 2014, ApJ, 783, 29
Fadda, D., Colditz, S., Fischer, C., et al. 2023, AJ, 166, 237
Fedriani, R., Tan, J. C., Telkamp, Z., et al. 2023, ApJ, 942, 7
Fischer, C., Beckmann, S., Bryant, A., et al. 2018, JAI, 7, 1840003
Fischer, C., Bryant, A., Beckmann, S., et al. 2016, SPIE, 9910, 991027
Fischer, C., Iserlohe, C., Vacca, W., et al. 2021, PASP, 133, 055001
Frerking, M. A., Langer, W. D., & Wilson, R. W. 1982, ApJ, 262, 590
Froese Fischer, C., & Saha, H. P. 1985, PhyS, 32, 181
Gaches, B. A. L., Bisbas, T. G., & Bialy, S. 2022, A&A, 658, A151
Hatchell, J., Fuller, G. A., & Richer, J. S. 2007, A&A, 472, 187
Hoare, M. G., Purcell, C. R., Churchwell, E. B., et al. 2012, PASP, 124, 939
Hofner, P., & Churchwell, E. 1996, A&AS, 120, 283
Iserlohe, C., Fischer, C., Vacca, W. D., et al. 2021, PASP, 133, 055002
Karska, A., Figueira, M., Mirocha, A., et al. 2025, A&A, 697, A186
Karska, A., Herpin, F., Bruderer, S., et al. 2014, A&A, 562, A45
Kim, S.-H., Martin, P. G., & Hendry, P. D. 1994, ApJ, 422, 164
Klein, R., Beckmann, S., Bryant, A., et al. 2014, SPIE, 9147, 91472X
Konigl, A., & Pudritz, R. E. 2000, in Protostars and Planets IV, ed. V. Mannings, A. P. Boss, & S. S. Russell, Vol. 759 (Univ. of Arizona Press)
Lacy, J. H., Knacke, R., Geballe, T. R., & Tokunaga, A. T. 1994, ApJL, 428, L69
Leurini, S., Wyrowski, F., Wiesemeyer, H., et al. 2015, A&A, 584, A70
Liu, M., Tan, J. C., De Buizer, J. M., et al. 2019, ApJ, 874, 16
Liu, M., Tan, J. C., De Buizer, J. M., et al. 2020, ApJ, 904, 75
Liu, X., Liu, T., Zhu, L., et al. 2024, RAA, 24, 025009
Lord, S. D. 1992, A new software tool for computing Earth's atmospheric transmission of near- and far-infrared radiation, NASA Technical Memorandum 103957, NASA
Luridiana, V., Morisset, C., & Shaw, R. A. 2015, A&A, 573, A42
Martin, W. C., Kaufman, V., & Musgrove, A. 1993, JPCRD, 22, 1179
Martins, F., Schaerer, D., & Hillier, D. J. 2005, A&A, 436, 1049
Mazzotta, P., Mazzitelli, G., Colafrancesco, S., & Vittorio, N. 1998, A&AS, 133, 403
McKee, C. F., & Tan, J. C. 2002, Natur, 416, 59
McKee, C. F., & Tan, J. C. 2003, ApJ, 585, 850
Molinari, S., Schilke, P., Battersby, C., et al. 2025, A&A, 696, A149
Molinari, S., Schisano, E., Elia, D., et al. 2016, A&A, 591, A149
Ossenkopf, V., & Henning, T. 1994, A&A, 291, 943
Purcell, C. R., Hoare, M. G., Cotton, W. D., et al. 2013, yCat, 2051
Seifert, W., Appenzeller, I., Baumeister, H., et al. 2003, SPIE, 4841, 962
Shepherd, D. S., & Churchwell, E. 1996, ApJ, 457, 267
Shu, F. H., Najita, J. R., Shang, H., & Li, Z. Y. 2000, in Protostars and Planets IV, ed. V. Mannings, A. P. Boss, & S. S. Russell, 789
Skrutskie, M. F., Cutri, R. M., Stiening, R., et al. 2006, AJ, 131, 1163
Tan, J. C., Beltrán, M. T., Caselli, P., et al. 2014, in Protostars and Planets VI, ed. H. Beuther, Vol. 149 (Univ. of Arizona Press)
Tanaka, K. E. I., Tan, J. C., & Zhang, Y. 2016, ApJ, 818, 52
Telkamp, Z., Fedriani, R., Tan, J. C., et al. 2025, ApJ, 986, 15
Temi, P., Hoffman, D., Ennico, K., & Le, J. 2018, JAI, 7, 1840011
Walsh, A. J., Macdonald, G. H., Alvey, N. D. S., Burton, M. G., & Lee, J. K. 2003, A&A, 410, 597
Watt, S., & Mundy, L. G. 1999, ApJS, 125, 143
Wenåker, I. 1990, PhyS, 42, 667
Wienen, M., Wyrowski, F., Menten, K. M., et al. 2015, A&A, 579, A91
Wood, D. O. S., & Churchwell, E. 1989, ApJS, 69, 831
Xu, F., Wang, K., & Liu, T. 2024, RAA, 24, 065011
Yang, B., Stancil, P. C., Balakrishnan, N., & Forrey, R. C. 2010, ApJ, 718, 1062
Zhang, Y., & Tan, J. C. 2011, ApJ, 733, 55
Zhang, Y., & Tan, J. C. 2018, ApJ, 853, 18
Zhang, Y., Tan, J. C., & Hosokawa, T. 2014, ApJ, 788, 166
Zhang, Y., Tan, J. C., & McKee, C. F. 2013, ApJ, 766, 86
Zhang, Y., Tan, J. C., Sakai, N., et al. 2019, ApJ, 873, 73
Zhu, Q.-F., Lacy, J. H., Jaffe, D. T., Richter, M. J., & Greathouse, T. K. 2008, ApJS, 177, 584
Zink, L. R., Evenson, K. M., Matsushima, F., Nelis, T., & Robinson, R. L. 1991, ApJL, 371, L85